Development of Robust Redox-Active Lyotropic Liquid Crystal Structures for Bioelectrodes

Wanli Liu, [a] *Jodie L. Hann,* [a] *Joshua S. White,* [b] *Adam Milsom,* [c] *Stephen Williams,* [a] *Leide P. Cavalcanti,* [d] *Iris S. Nandhakumar,* [b] *Emily R. Draper,* [e] *Simon E. Lewis,* [a] *Mirella Di Lorenzo* [f] *and Adam M. Squires* [*a]

AUTHOR ADDRESS

a. Department of Chemistry, University of Bath, Bath BA2 7AY, U.K.

b. School of Chemistry, University of Southampton, Southampton, SO17 1BJ, U.K.

c. School of Geography, Earth and Environmental Sciences, University of Birmingham, Edgbaston, Birmingham B15 2TT, U.K.

d. ISIS Neutron and Muon Source User Office, Science and Technology Facilities Council, Rutherford Appleton Laboratory, Harwell Oxford, Didcot OX11 0QX, U.K.

e. School of Chemistry, University of Glasgow, Glasgow G12 8QQ, U.K.

f. Department of Chemical Engineering, and Centre for Bioengineering and Biomedical Technologies (CBio), University of Bath, BA2 7AY, U.K.

KEYWORDS

Small-angle neutron scattering, in-situ electrochemical experiment, biosensing, lyotropic liquid crystal

ABSTRACT

The fabrication of stable and highly performing enzyme-based electrodes is key for the effective generation of biodevices and bioelectronics, such as electrochemical biosensors. In this context, redox-active lyotropic liquid crystals based on 3D nanomaterials, known as lipid cubic phases (LCP), hold great potential due to the large specific surface area and the possibility to be functionalized. In this study, we functionalized a monoolein (MO) LCP matrix by incorporating an amphiphilic redox shuttle within its matrix with the aim to enhance the electrochemical performance of a glucose oxidase (GOx) based electrode and we investigated the stability of the overall system. The use of dodecyl(ferrocenylmethyl)dimethylammonium bromide (Fc12-Br) resulted in an electroactivity loss with time of the resulting Fc12-Br/MO electrode, probably due to the formation of a passivating layer between the bromide counterions and the electrode surface. Hence, bromine (Br^-) was replaced with hexafluorophosate (PF_6^-), leading to Fc12-PF_6/MO. Both structures were used for GOx entrapment and the resulting electro-activity towards glucose was assessed. Though the sensitivity obtained with the Fc12-Br/MO/GOx and Fc12-PF_6/MO/GOx systems was comparable, the latter showed superior stability over time, with more than 80% activity retained for > 20 days. Moreover, when the concentration of the Fc12 redox shuttle within the cubic phase was increased by 10, a 4 times greater current density was generated. Consequently, the Fc12-PF_6/MO electrode shows superior stability and performance than previously reported redox lyotropic LCP systems, thus paving the way for promising applications in enzyme-based biodevices.

INTRODUCTION

Biosensors are expecting to play a pivotal role in the future of healthcare, enabling personalized therapies, effective chronic disease management, early diagnostics and point-of-care monitoring.[1] Due to unique features, such as selectivity and specificity, enzymes are particularly attractive bioreceptors in such systems, , and their use, along with an electrochemical-based transduction, enables the development of miniaturized and simple-to-use devices .[2-4] In enzyme-based electrochemical sensors, the effective electron transfer between the redox center of the enzyme and the electrode is key. As a direct electron transfer between enzyme and electrode may be challenging, and highly depending on the enzyme used, the use of redox mediators to facilitate the electron transfer can prove to be more effective.[5]

To date, a series of approaches have been developed to immobilize enzymes at transducer surfaces while achieving efficient electron transfer processes. [6] Nanomaterials with continuous nano-networks are promising candidates, such as graphene, carbon nanotubes (CNTs) and metal oxides. [7-9] However, the electrode fabrication processes are in-efficient, which often adopt 'bottom-top' approaches, leading to time-consuming synthetic and doping steps for the bioelectrodes. In addition, health effects about employing these nanomaterials have been reported, in particular, the biocompatibility and the carcinogenicity of CNTs. [10, 11] Therefore, there is a need for the development of new nanomaterials for bioelectrode fabrication.

Previous research has focused on the use of flexible conductive polymers to wire the enzymes onto the electrodes, with common substrates including poly(3,4-ethylenedioxythiophene/polystyrene sulfonic acid) (PEDOT:PSS).[12] Setti et al[13] fabricated electrodes with PEDOT:PSS/GOx matrixes through thermal inkjet printing, which while promising, suffered from stability issues (e.g. PEDOT:PSS dissolves in electrolyte) and involved

the redox mediator in solution, which cannot be practical in real applications.[14] Yu et al[15] recently realized a PEDOT:PSS hydrogel system that attaches glucose oxidase (GOx) within the network onto the carbon nanotube fiber modified electrodes. It demonstrated novel glucose sensing ability in the absence of additional redox mediators. However, the mechanistic details remains many conflicts and requires further studies. [15, 16] Generally speaking, conductive polymers offer several merits including flexibility, low-cost and adjustable properties. Meanwhile, confinement of the polymer at the electrode surface can be challenging, in addition to temperature and long-term stability issues.[12, 17, 18] Biosourced lyotropic liquid crystals that are meta-stable over a range of temperatures in excess aqueous conditions show distinctive merits in enzyme. [19]

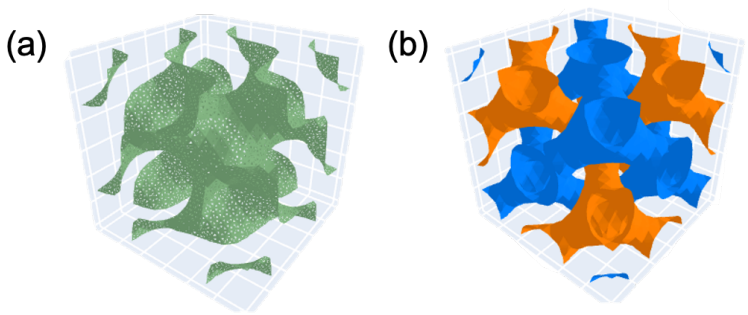

Figure 1. Lipid cubic phase formed by 1-monoolein in excess aqueous condition adopting double-diamond (Pn3m) symmetry [20]: (a) the curved lipid bilayer, and (b) two non-intersecting water channels situating at either side of the lipid bilayer.

We recently reported the use of a redox-active lyotropic liquid-crystal structure for the effective immobilization of glucose oxidase (GOx). [21] The system is based on a three-dimensional nanomaterial known as a lipid cubic phase (LCP), as shown in **Figure 1a**. The lipid cubic phase is formed by type II lipids, [22] organized into a bilayer with a unique triply periodic minimal surface

(TPMS).[23] This structure adopts a continuous labyrinth network structure, periodic in three spatial dimensions,[24] with two non-intersecting aqueous channels, located on either side of the lipid membrane, as illustrated in **Figure 1b**. The structure is naturally occurring and has been observed in various types of biological systems. [25-27] 1-monoolein (MO) is one of the typical lipids that undergoes self-assembly transformation into cubic phase structures in excess aqueous conditions. [22] Owing to its biocompatibility and ready availability, MO has been extensively used in protein crystallization[28, 29], drug delivery[30-32] and biosensing[33-35].

We have successfully demonstrated the functionalization of MO LCP with an amphiphilic redox probe, dodecyl(ferrocenylmethyl)dimethylammonium bromide (Fc12-Br), to enhance the electroactivity of the entrapped GOx enzyme. Nonetheless, the activity of the Fc12-Br/MO/GOx bioelectrode rapidly decayed after 7 days, hindering practical applications. We hypothesised that this might be predominantly due to the instability of the redox probe because in other studies the LCP without Fc12 was found to enhance the stability of GOx at room temperature. [36, 37] Causes for this instability could be : a) Fc12-Br leaching at the interface into the bulk environment; [38] b) Fc12-Br inducing a localized phase transition away from the Pn3m structure into a phase such as the two-dimensional lamellar L_α phase which would show retarded 3D diffusivity;[39] and c) other processes, such as a surface adsorption or reaction, as previously reported. [40] To develop a stable system for practical applications, it is important to discriminate between these alternatives, for example by localizing the Fc12-Br molecules during electrochemical reactions. Accordingly, in this work we performed in-situ small-angle neutron scattering (SANS), adopting the set-up from Randle et al[41] and Draper.[42]

Neutron beams interact differently to matter compared to X-ray beams,[43] which leads to intrinsic differences in values of scattering length density (SLD) for neutrons compared to X-rays. [44] With

appropriate contrast-matching, some features that might be concealed in X-ray scattering could be revealed under SANS. In previous work, Van't Hag et al[45] demonstrated contrast matching the scattering signal of deuterated monoolein (d-MO) with D_2O, shedding light on the localization of the additive proteins within the LCP. The investigation on structural evolution of a diamond-type LCP triggered by guest components by means of SANS and SAXS is reported by Angelov et al.[46]

In this work, we first study the localization of Fc12-Br molecules within LCP using in-situ contrast-matched SANS experiments; from this we rule out some hypothesized mechanisms for activity decay; and finally, we demonstrate a successful solution to the activity decay issues. The resulting redox-active LCP system, hosting GOx, demonstrated glucose biosensing activity, with more than 80% activity retained after 20 days of operation, thus encouraging uses in relevant biomedical applications, such as glucose monitoring.

METHOD

Materials

Monoolein-d_{33} (1-oleoyl-*rac*-glycerol-d_{33}, isotopic purity of 94% ± 2%) was purchased from ANSTO, monoolein (1-oleoyl-rac-glycerol) was purchased from Croda (Cithrol GMO HP-SO-LK, purity >96%), dodecyl(ferrocenylmethyl)dimethylammonium bromide (purity >97%) and silver hexafluorophosphate (purity>98%) were purchased from Tokyo Chemical Industry ltd. Glucose oxidase (E.C.1.1.3.4 from *Aspergillus Niger*), D-(+)-glucose, sodium phosphate dibasic, sodium phosphate monobasic, sodium hydroxide, sodium deuteroxide solution, hydrochloric acid, hydrochloric acid-d solution and deuterium oxide were acquired from Sigma Aldrich.

Solution preparations

In-situ SANS experiments: Deuterated 100mM phosphate buffer (PB) solutions (pD=7.0) were prepared by dissolving appropriate amount of sodium phosphate diabasic and sodium phosphate monobasic in deuterated water D_2O, followed by adjusting the pH with sodium deuteroxide NaOD and deuterium chloride DCl. The non-deuterated 100mM phosphate buffer solutions (pH=7.0) were prepared in Millli Q water (18.2 MΩ cm^{-1}, Millipore, Bedford, MA, USA) and the pH was adjusted using sodium hydroxide NaOH and hydrochloric acid HCl.

Ex-situ experiments: Glucose solutions were prepared in non-deuterated 100 mM phosphate buffer solutions (pH=7.0) at least 24 h before the experiments. [47]

Synthesis of dodecyl(ferrocenylmethyl)dimethylammonium hexafluorophosphate

The synthesis protocol from Facci *et al*[48] was adopted. Fc12-Br was dissolved in a $NaPF_6$ saturated 50/50 ethanol/water (v/v) solution, after which 1.2 molar equivalence of $AgPF_6$ was added. The mixture was stirred for 5 min prior to the addition of dichloromethane for phase separation. The organic layer was then collected, dried over $MgSO_4$, and concentrated via a rotary evaporator. To obtain the final product, the mixture was placed in an ice bath and recrystallized from 50/50 water/methanol, giving brilliant yellow platelets.

Cubic phase preparation

The procedure of preparing surfactant doped monoolein cubic phase was adapted from Tyler *et al*. [49] Appropriate amounts of dry monoolein and Fc12-Br or Fc12-PF6 powder were weighed accordingly and co-dissolved in EtOH/Chloroform (1:1, v/v) mixture. The samples were dried under a N_2 gas purge over 24 hours and vortexed in a 40˚C water bath for 10 minutes. The homogeneity was then assessed by macroscopic inspection. The protocol was used to prepare dry Fc12-Br/d-MO, Fc12-Br/MO, Fc12-PF_6/MO and Fc12-PF_6/d-MO lipid mixtures.

The bulk cubic phase pastes without GOx were prepared by mixing the molten dry lipidic mixture with non-deuterated 100mM PB solutions in the ratio lipid: aqueous 60/40 (w/w). The cubic phase pastes hosting GOx were prepared according to Nazaruk *et al*. [50] In short, 5 mg of GOx was dissolved in 100 µL of non-deuterated 100 mM PB solution (pH=7.0) to yield 50 mg mL^{-1} of GOx, after which 40 µL of the enzyme solution was mixed with 60 µL of molten dry lipidic matrix (Fc12-Br/MO or Fc12-PF_6/MO).

Electrochemical set-up

Cyclic voltammetry (CV) and multi-step chronoamperometry (CA) measurements were performed using PalmSens EmStat3$^+$ (Alvatek Ltd.).

***In-situ SANS experiments*:** The experimental set-up designed by Randle *et al* was adopted. [41] A modified LabOmak UF-spectro-electrochemical cell was used to conduct all the in-situ experiments. The cell resembling a 2-electrode set up has Pt mesh working and counter electrodes, and a pseudo reference electrode made of a Pt wire. A custom-made 2 mm path length quartz cuvette (Quartz Scientific Glassblowing Ltd., UK) was used to hold the electrodes and the electrolyte in place. To fabricate the working electrode with cubic phases, approx. 60 mg samples of cubic phase pastes were applied and spread evenly to cover the electrode surface over an area of approximately 15 × 10 mm. The modified electrode was soaked in the electrolyte for 20 min to allow equilibration before experiments.

***Ex-situ experiments*:** A three electrode set-up was adopted for the ex-situ experiments with a gold disk electrode (Ø=2 mm), a Pt mesh counter electrode and Ag|AgCl (3M KCl) as the reference electrode. Prior to electrode fabrication, the Au disk working electrode was polished with two grades of Al_2O_3 powders (0.3 µm and 0.1 µm) on wet polishing cloths, followed by sonication in

water for 5 mins then in EtOH for another 5 mins. The working electrode was further activated by running cyclic voltammetry at 0.1 V s^{-1} in 0.5 M H_2SO_4 for 15 cycles between 0 and 1.6 V vs Ag|AgCl (3 M KCl).

The working electrode fabrication was conducted as per Liu *et al.* [21] Two strips of tapes with measured thickness (200µm) were attached to either side of the electrode surface to control the film thickness prior to electrode fabrications. 20 mg of cubic phase was deposited onto the electrode surface, gently pressed, and the excess materials removed/scraped off using a spatula. The modified electrode was then soaked in the electrolyte for 20 min before experiments for equilibration.

Electrochemical characterization of Fc12 doped MO cubic phases

In-situ stability test: Two types of in-situ electrochemical experiments were performed: chronoamperometry and continuous cyclic voltammetry. Chronoamperometry was carried out by holding the potential at 0.7 V vs Pt wire at pH7 for 1 hour. The 0.7 V applied against Pt wire is approximately 0.8 V vs Ag|AgCl (3 M KCl). This value was normalized by measuring the shift of 0.1 M ferricyanide in acetonitrile/water (10/90, v/v) in the three-electrode set-up using Pt wire or Ag|AgCl (3 M KCl) as the reference electrode. (see SI Figure 2). Continuous cyclic voltammetry measurements were applied to study the electrochemical stability for Fc12-Br/dMO. The potential was swept between 0.0 V and 0.7 V vs Pt wire at 0.1 V s^{-1} for 1 hour.

Ex-situ stability test: Continuous cyclic voltammetry measurements were used to examine the electrochemical stability for both Fc12-Br/MO and Fc12-PF_6/MO. The potential was swept between 0.0 V and 0.85 V vs Ag|AgCl at 0.01 V s^{-1} for 250 cycles, approximately 70 minutes.

***Diffusivity study of Fc12-PF6 doped MO cubic phases*:** Cyclic voltammetry measurements using the *ex-situ* three-electrode set-up were carried out. The potential was swept between 0.3 V and 0.85 V versus Ag|AgCl (3 M KCl). Voltammograms with 5 different voltage sweeping rates were recorded: 0.01 V s^{-1}, 0.025 V s^{-1}, 0.05 V s^{-1}, 0.075V s^{-1} and 0.1 V s^{-1}. The order of voltage sweeping rates was randomized to minimize any unexpected time effect from the system.

The Randles-Sevick equation (Equation 1) was applied to calculate the diffusion coefficient of the redox probe[51] :

$$\boldsymbol{i_p = 0.4463nFAC\left(\frac{nFvD_0}{RT}\right)^{\frac{1}{2}}} \quad (\boldsymbol{Equation\ 1})$$

where i_p is the maximum current (μA), n is the number of electrons involved in the redox reaction, F is the Faraday constant (96485.3321 s A mol^{-1}), A is the electrode surface area (cm^{-2}), C is the concentration of the Fc12-PF_6 (mM), D_0 is the diffusion coefficient (cm^2 s^{-1}), v is the voltage scan rate (V s^{-1}), R is the gas constant (8.3145 J mol^{-1} K^{-1}) and T is the temperature (K).

***Fc12-PF6/MO/GOx biosensing and stability test*:** The electrocatalytic activity of Fc12-PF_6/MO/GOx was studied by cyclic voltammetry at 0.1V s^{-1} in the absence and presence of glucose with varying concentrations within the range of 0-9 mM.

A calibration curve was obtained by measuring the chronoamperometry response of the Fc12-PF_6/MO/GOx electrode to increasing concentrations of glucose, ranging from 0 to 20 mM, at an applied potential of 0.85 V vs Ag|AgCl (3 M KCl).

To test the stability of the bioelectrode, the amperometric response of the Fc12-PF_6/MO/GOx bioelectrode to 6 mM glucose was assessed by CA at an applied potential of 0.85 V vs Ag|AgCl

(3 M KCl). After measuring the activity, the bioelectrode was stored in a PB solution (pH 7) at room temperature (20˚C).

SANS measurement

The *in-situ* study of the electrochemical behavior of Fc12-Br/d-MO was performed on the ZOOM SANS beamline (STFC ISIS Pulsed Neutron Source, Oxfordshire, UK). The beamline was run in time-of-flight mode with incident wavelengths from 1.75 Å to 16.5 Å. The sample detector distance (SDD) was 4 m, with beam size of 8 mm x 6mm and a typical q-range from 0.004 $Å^{-1}$ to 0.7 $Å^{-1}$. Exposure time was set as 30 min each frame. For *in-situ* data, the data was sliced every 15 min to resolve any time-evolving features. The scattering intensity was normalized to the absolute scale calibrating against the intensity of a polystyrene standard. Data reduction was made using Mantid Project.[52]

SAXS measurement

The Anton Paar Multi-Paste cell was used to hold varying bulk cubic phase pastes for SAXS measurements. The sample holder with 4 × 5 grids (each has dimension of 11×11 mm) comprises of 2 metal plates sandwiching the samples between two Kapton sheets. For sample preparations, approx. Ten mg of cubic phase paste was transferred into each cell of the sample holder to give a layer approximately 1.6 mm thick, and topped with 10μL of 100mM PB (pH=7.0) to ensure excess aqueous conditions.

The 2D SAXS patterns of the samples were collected on a Dectris Eiger detector from an Anton Paar SAXS Point 2.0, using Cu source K_α radiaiton (λ=1.54 Å), with beam diameter approximately 1 mm, sample-detector distance of 572 mm, and acquisition time 10 mins for each sample. The

data reduction of 2D to 1D radial profile was performed using Anton Paar SAXSAnalysis software by azimuthal integration of 330˚.

RESULTS AND DISCUSSION

Stability of Fc12-Br/MO

The electrochemical reversibility of the redox probe over time in a mediated-electron-transfer system is of paramount importance for practical applications. Therefore, to assess the long-term stability of the 10%Fc12-Br/MO electrode a continuous cyclic voltammetry measurement was conducted (as shown in **Figure 2**).

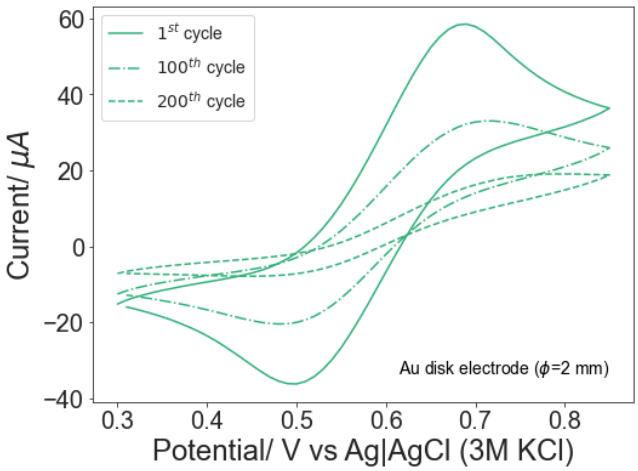

Figure 2. Cyclic voltammograms for 10%Fc12-Br/MO (wt%) in 100 mM PB (pH=7.0) recorded at 0.1 V s^{-1} at 1st, 100th and 200th continuous redox cycles respectively.

During the 1st redox cycle, the voltammogram adopts a quasi-reversible shape[53] and the ratio between anodic peak and cathodic peak (i_{pa}/i_{pc}) is approx. 1. However, as the redox cycling continued, the shape of the voltammogram began to change. At the 100th cycle, the magnitude of

both the anodic and cathodic current decreased dramatically, although the system was still quasi-reversible at 100th cycle, and the value of the peaks separation (E_{pa}-E_{pc}) did not change. The magnitude of the currents kept decreasing as the redox cycling proceeded. At the 200th cycle, the shape of the voltammogram was further compressed compared to the 1st cycle. It is also noteworthy that the Fc12-Br lost the reversibility, leading to the disappearance of the cathodic peak.

Three hypotheses were considered to interpret this result. One hypothesis is that the Fc12-Br exits the bilayer and dissolves in the aqueous regions as micellar aggerates. [38] Another possibility is that the Fc12-Br induces a localized phase transition away from the Pn3m structure; the interfacial curvature of lipid membranes could be flattened leading to a 3D-2D phase transition of Pn3m-lamellar (L_α), [54] which subsequently reduces the diffusivity of Fc12-Br.[39] Finally, another option is that other processes occur, such as adsorption with the electrode surface leading to a passivating layers. [40]

To discriminate between these mechanisms, real-time SANS data were collected during electrochemical cycling, with and without contrast-matching of the majority lipid component. The scattering data would inform on the localisation of the electroactive surfactant, thus revealing any underlying mechanisms associated with the degradation in performance.

Contrast matching of 10%Fc12-Br/d-MO

Initially, SANS experiments were performed on d-MO without Fc12-Br in excess of H_2O and D_2O PB solutions respectively, as shown in **Figure 3a**, to demonstrate contrast matching the SLD of d-MO.

In excess H_2O PB solution, the d-MO pastes exhibited characteristic features of a double-diamond cubic phase with Pn3m symmetry. Two Bragg peaks are seen at q ~ 0.093 and 0.113 Å^{-}

[1], which correspond to the √2 and √3 Miller indices.[22] The lattice parameter of the d-MO in H_2O PB was calculated as 95.4 Å, consistent with literature values. [49] Conversely, in excess of D_2O PB solution, no Bragg peaks were observed. The disappearance of scattering signals is attributed to the scattering length densities (SLD) of bulk D_2O PB solution and d-MO were matched.[45] Therefore, the contrast matching of SLD in d-MO enables a distinction between the signals from the additive Fc12-Br.

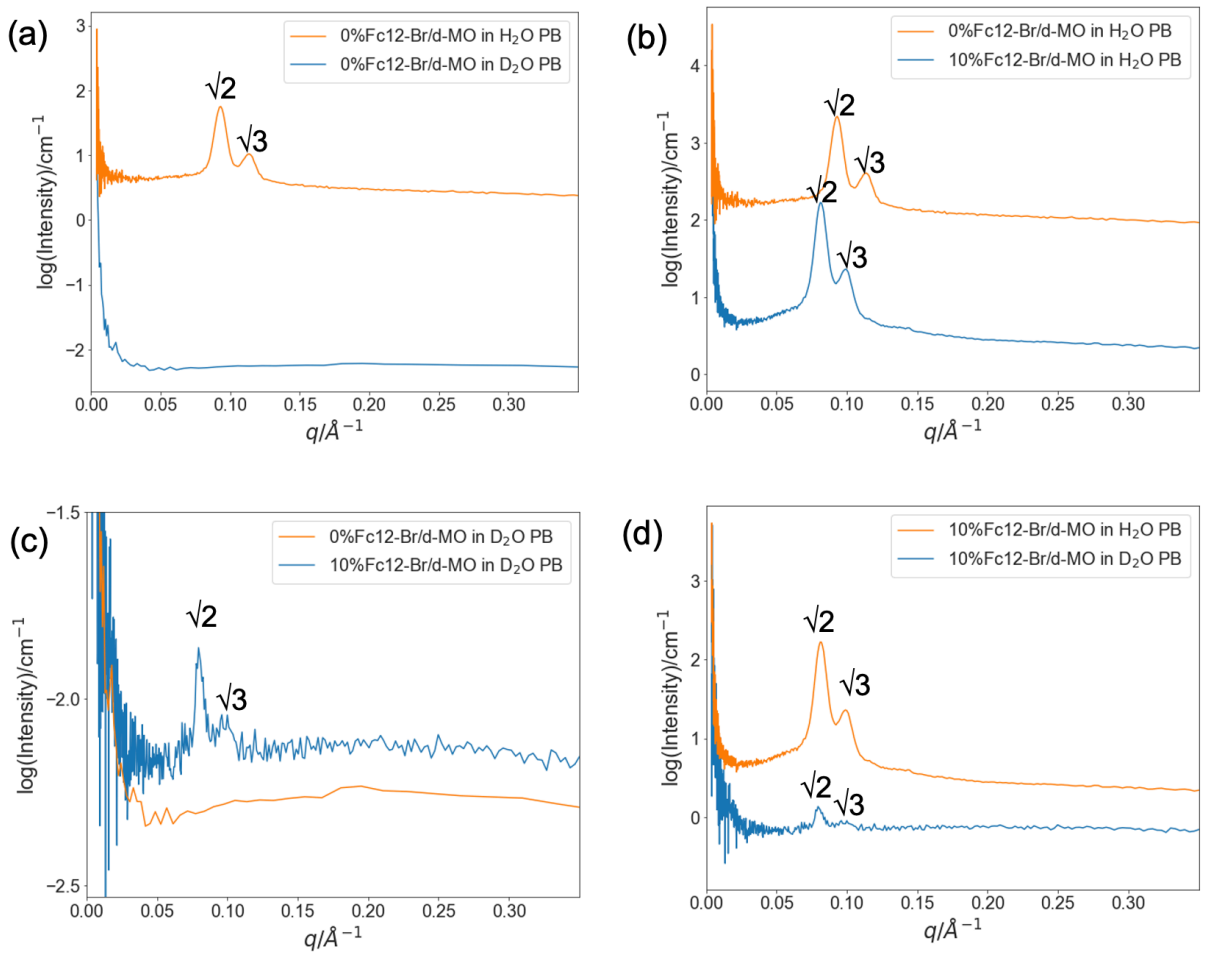

Figure 3. SANS patterns for (a) 0% (w/w) Fc12/d-MO cubic phase in H_2O PB solution (pH=7.0) without contrast matching and in D_2O PB solution (pD=7.0) with contrast matching of $SLD_{d\text{-}MO}$; (b) 0% (w/w) Fc12-Br/d-MO and 10% (w/w) Fc12-Br/d-MO cubic phase in H_2O PB solution without contrast matching; (c) 0% (w/w) Fc12-Br/d-MO and 10% (w/w) Fc12 cubic phase in D_2O PB solution with contrast matching; (d) 10% 9w/w) Fc12-Br/d-MO cubic phase in H_2O PB solution (pH=7.0) without contrast matching and in D_2O PB solution (pD=7.0) with contrast matching of $SLD_{d\text{-}MO}$.

The SANS pattern of 10% (w/w) Fc12-Br/d-MO(w/w) in H_2O PB is shown in **Figure 3b**. Both d-MO with and without 10% (w/w) Fc12-Br adopted Pn3m symmetry. However, the peak positions of 10% (w/w) Fc12/d-MO were shifted towards the low-q region, with q values of 0.082 and 0.099 $Å^{-1}$. The lattice cell dimension was estimated to be 110.3 Å. This implies that the lattice cell dimension of the mesophase is increased upon incorporating 10% (w/w) Fc12-Br. The swelling effect might be due to the electrostatic repulsions between the Fc12-Br molecules that inserted at the lipid/aqueous interface, which caused the curvature of the lipid membrane to flatten. [55] The lattice parameter of 10% (w/w) Fc12-Br/d-MO obtained from SANS measurements is slightly greater than our previously acquired SAXS data, 99.3 Å.[21] This result could be due to the uncertainties in preparing samples at microliter scales. The SANS pattern of $SLD_{d\text{-}MO}$ contrast matched 10%Fc12/d-MO in D_2O PB is displayed in **Figure 3c**. Notably, two peaks at q~ 0.082 and 0.099 $Å^{-1}$ persisted after contrast matching (see **Figure 3d)**. These peaks correspond to the incorporated Fc12-Br molecules, suggesting that the additives within the mesophase adopted the same symmetry as the d-MO host medium. A similar additive effect upon incorporation of membrane proteins into cubic phases has been reported. [45]

By combining these results, it can be concluded that the Fc12-Br molecules are incorporated into the LCP mesophase, and adopt the same spatial arrangement as the host medium, d-MO cubic phase. If the Fc12-Br were to leave the d-MO cubic phase or induce a local phase change during *in-situ* electrochemical experiments, the SANS patterns would exhibit significant changes comparing to those before electrochemical bias.

In-situ study of 10%Fc12-Br/d-MO

The chronoamperometry *in-situ* SANS experiment was performed in D_2O PB to screen the scattering signals from d-MO. As shown in **Figure 4a**, the peak positions of the contrast matched 10%Fc12-Br/d-MO did not move during the electrochemical test. After applying the electrochemical bias, the SANS patterns of 10%Fc12-Br/d-MO in H_2O PB was collected and compared to that before the chronoamperometry measurement (see **Figure 4b**); both peak position and the relative intensity for each Bragg peak did not change. As shown in **Figure 4c**, the lattice dimension of the 10%Fc12-Br/d-MO according to the q values of the Bragg peaks was consistent over time. Therefore, no phase transition occurred after holding an oxidative potential for 1 hr, and the 10%Fc12-Br/d-MO remained in the double-diamond cubic phase. As such, it was concluded that no significant leaching of the Fc12-Br molecules from the cubic phase occurred throughout the chronoamperometry measurement. A follow-up chronoamperometry data set on the same 10%Fc12-Br/d-MO coating was collected (see **Figure 4d**) and the transient current was found to drop by over 60%. Although the Fc12-Br molecules did not escape from the mesophase, the activity degradation of the redox probe was still observed.

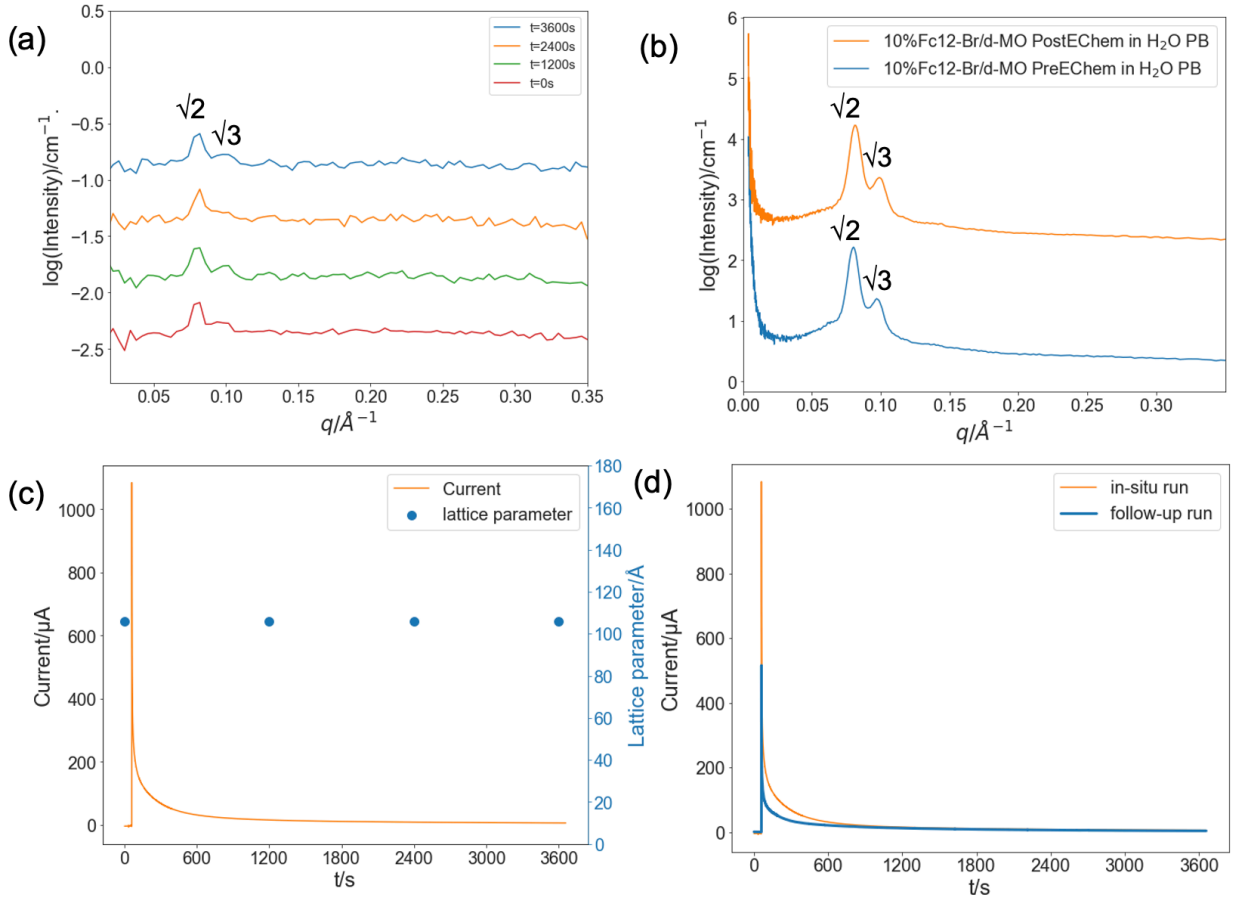

Figure 4. SANS patterns for (a) *in-situ* experiments of contrast-matched 10%Fc12-Br/d-MO over the course of continuous redox cycling; (b) non-contrast matched 10%Fc12-Br/d-MO before and after the multi-step chronoamperometry, (c) multi-step chronoamperometry of contrasted matched 10%Fc12-Br/d-MO and the lattice parameter of the 10%Fc12-Br/d-MO within 1hr during the *in-situ* experiment, and (d) chronoamperometries of 10%Fc12-Br/d-MO in D_2O PB during the *in-situ* experiment and the repeat measurement after the *in-situ* experiment (follow-up run)

To assess the underlying mechanism of signal decay for 10%Fc12-Br/d-MO over continuous redox cycling, an *in-situ* SANS experiment was also performed to the system during repetitive cyclic voltammetry for 1 hour.

As shown in **Figure 5a**, the Bragg peak positions of 10%Fc12-Br/d-MO did not shift during the redox cycling, which is similar to what observed with the chronoamperometry experiment. The cyclic voltammograms collected at the 1st, 100th and 200th cycles are shown in **Figure 5b**. It is clear that the shape of the cyclic voltammetry changed significantly. Comparing to the 1st cyclic voltammogram, the anodic peak currents dropped by 65.8% after 100 cycles and by 75.1% after 200 cycles. The anodic peak currents (i_{pa}) of Fc12-Br and the calculated lattice parameter of 10%Fc12-Br/d-MO during the continuous redox cycling are shown in **Figure 5c**. After the first 600s the anodic peak currents decayed by 52.1%, and it subsequently reached a steady state. Meanwhile, the lattice parameter of the 10%Fc12-Br/d-MO stayed at 110.3 Å during the *in-situ* experiment, suggesting that no leaching from the cubic phase of Fc12-Br molecules had occurred.

Nonetheless, the color of the Pt working electrode became darker after the electrochemical tests, suggesting that an interaction had occurred between Br^- ions in the water channels and the metal electrode. The electrodeposition of Br^- onto noble metal surface, for example Au and Pt, has been reported elsewhere.[56, 57] The resultant monolayer might act as an insulation layer that inhibits the $Fc12^+$ from further interaction with the Pt working electrode, and thus leading to a reduction in the current peaks after each CV cycles. Since Br^- ions may be the cause of this phenomenon, salt metathesis for Fc12-Br to replace the counter anion by $[PF_6]^-$ was considered.

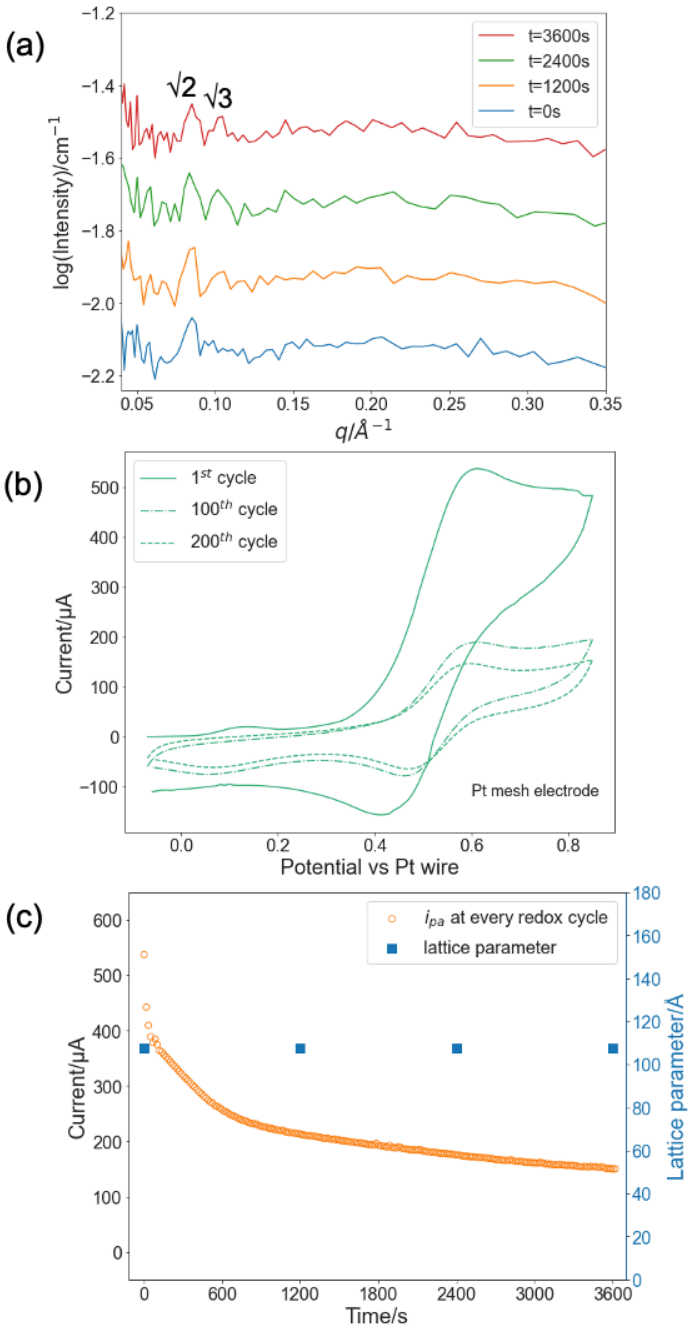

Figure 5. Continuous redox cycle *in-situ* experiments in D_2O PB: (a) SANS patterns of 10%Fc12-Br/d-MO; (b) cyclic voltammograms of 10%Fc12-Br/d-MO recorded at 0.1V s^{-1} at 1st, 100th and 200th redox cycle respectively; (c) the anodic peak current (i_{pa}) at every redox cycle and the calculated lattice parameter of 10%Fc12-Br/d-MO over 1 hour of continuous redox cycling

Fc12-PF_6/MO characterizations

First, the phase integrity of the monoolein cubic phase upon addition of Fc12-PF_6 into MO was assessed. The SAXS pattern of 10%Fc12-PF_6/MO in excess H_2O PB is shown in **Figure 6a**. The MO self-assembly material maintained Pn3m cubic phase symmetry with the presence of 10%Fc12-PF_6. However, instead of causing the lattice dimension of the MO cubic phase to swell, as observed in the case of 10%Fc12-Br, the lattice parameter of the Fc12-PF_6 doped MO shrank slightly from 95.4 Å (undoped MO LCP) to 93.1Å; the Bragg peaks of 10%Fc12-PF_6 were slightly shifted to the high-q regions. The SANS results (**Figure 6b)** also show this, where the presence of 10%Fc12-Br caused the hosting cubic phase to swell whereas 10%Fc12-PF_6 led to shrinkage of the mesophase.

The localization of Fc12-PF_6 within MO cubic phase was assessed by SANS. **Figure 6c** shows a comparison of the d-MO contrast-matched SANS patterns collected for 10%Fc12-PF_6/d-MO 10%Fc12-Br/d-MO and d-MO. Two characteristic Bragg peaks were observed for 10%Fc12-PF_6/d-MO after contrast-matching, which confirmed that the additive molecules adopted Pn3m symmetry within the cubic phase. Additionally, the peak positions of the contrast matched SANS pattern were aligned with the non-contrast matched assay (see **Figure 6d**), which suggests that the Fc12-PF_6 molecules followed the same symmetry as the MO and had been successfully incorporated into the mesophase.

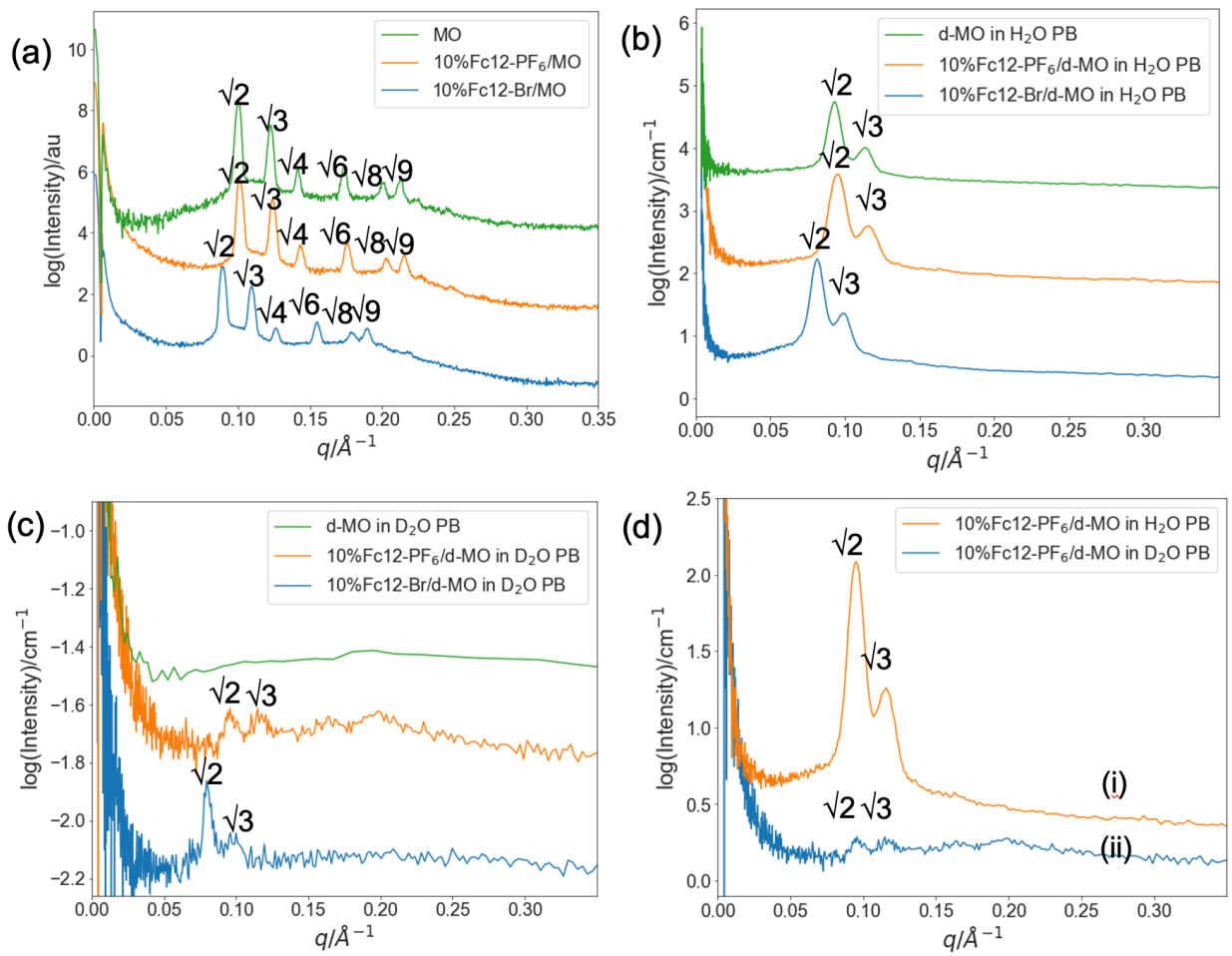

Figure 6. (a) SAXS patterns for MO, 10%Fc12-PF6/MO and 10%Fc12-Br/MO in excess H_2O PB, SANS patterns for d-MO, 10%Fc12-PF_6 and 10%Fc12-Br in excess (b) H_2O PB; (c) D_2O PB, and (d) SANS patterns for 10%Fc12-PF6/d-MO in excess (i) H_2O PB and (ii) D_2O PB

The relative intensity ratios between √2 and √3 Bragg peaks vary between 10%Fc12-Br/d-MO and 10%Fc12-PF_6/d-MO after contrast matching, and are 3:1 and 2:1 respectively. The contrast matched SANS pattern of Fc12-PF_6 may predominantly be a result of the PF_6^- counterions in the water channels, because the F atoms have large SLD against the incident neutron beam. The

relative intensity change reflects the different location of the scattering centers within the unit cell.

28

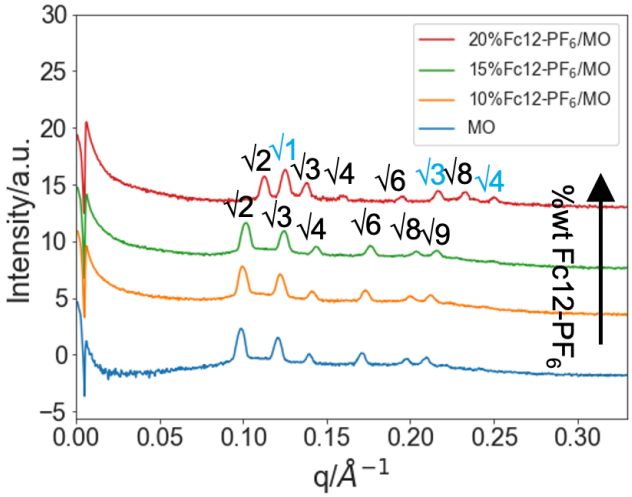

Figure 7. SAXS patterns of MO incorporating varying %wt Fc12-PF_6 in excess PB solution condition. The Bragg peaks for Pn3m cubic phases are indexed as √2, √3, √4, √6, √8 and √9; the inversed hexagonal phases (H_{II}) are indexed as √1, √3 and √4.

The additive effect of varying the wt% Fc12-PF_6 on the dimensionality of a MO cubic phase was investigated using SAXS. As shown in **Figure 7**, as the wt% Fc12-PF_6 increases, the Bragg peaks of the material shift towards high-q region, suggesting that a shrinkage of the lattice cell parameter of the cubic phase. The MO cubic phase with Pn3m symmetry demonstrates the Fc12-PF_6 uptake limit of 15% (wt%); at 20% Fc12-PF_6, a mixed phase consists of Pn3m cubic phase and inversed hexagonal phase (H_{II}) was formed.

Fc12-Br and Fc12-PF_6 have opposite effects on the lattice parameter of the MO cubic phase, with the former inducing swelling whereas the latter leads to shrinkage. This might be due to the varying nature of the counter anions, Br^- and PF_6^- . It has been found that anions have considerable

impacts on the curvature of a lipid membrane, which can either be "kosmotropic" or water-structure making, or "chaotropic" (structure breaking) effect.[58] Kosmotropic ions generally promote increased Gaussian curvature in lipid cubic phases, causing the lattice cell dimension to shrink. The chaotropic ions promote flatter interfaces with lower curvature, which leads to increased lattice cell dimension. [59] The Br^- ion is generally considered to be kosmotropic, while the $[PF_6]^-$ ion is more chaotropic.[60] However in this case, they have the opposite effects to what expected, with PF_6^- promoting a decrease in lattice parameter and then the formation of H_{II}, associated with more highly curved interfaces [55] and Br^- doing the opposite.

The electrochemical activity of 10%Fc12-PF_6 was studied *ex-situ* by CV to test the stability over repeated redox cycling, and to investigate the diffusivity of the redox probe. The voltammograms collected at 0.1V s^{-1} are shown in **Figure 8a**. In contrast to 10%Fc12-Br (**Figure 2**), the 10%Fc12-PF_6 system maintains most of its peak current and cyclic voltammogram shape characteristic of reversible electron transfer up to 200 cycles; the 70% activity loss observed in 10%Fc12-Br is here absent , thus confirming the hypothesis of Br^- reactivity.

The cyclic voltammogram shows an initial additional smaller pair of redox peaks at 0.42 V/0.31 V, which disappear within the next cycles. Our previous work[21] suggests that these peaks arise from Fc12 micelles dissolved in aqueous channels, whereas the main higher potential peaks at approx. 0.6 V/0.5 V corresponded to the molecules being incorporated into the lipid membrane.

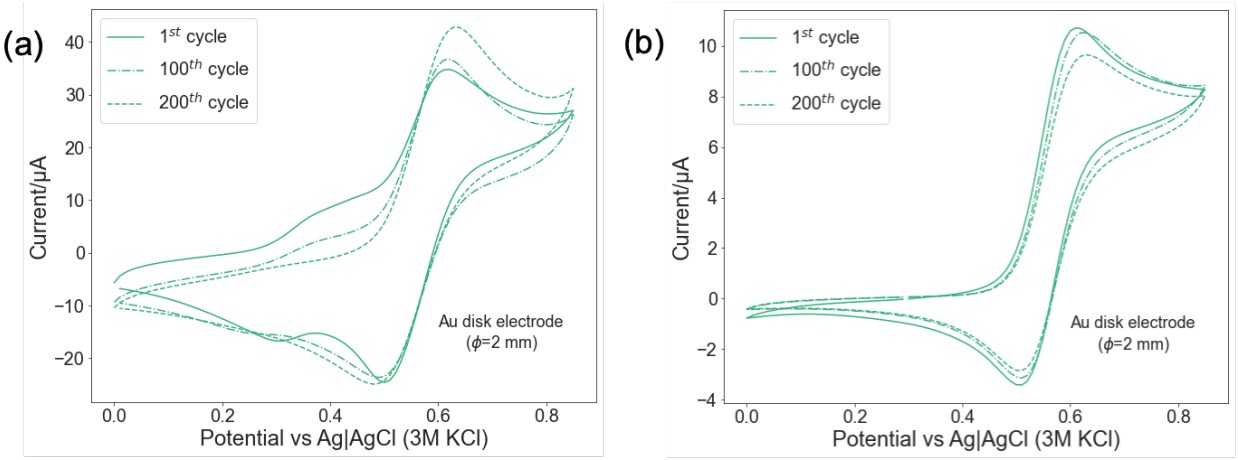

Figure 8. Cyclic voltammograms of (a) 10%Fc12-PF_6/MO and (b) 2%Fc12-PF_6/MO modified Au disk electrode recorded at 0.1 V s^{-1} in H_2O PB at 1st, 100th and 200th cycle.

By sweeping the potential between 0 and 0.85 V continuously over 200 cycles, the currents at 0.42 V/0.31 V gradually decreased whereas the magnitude of the currents from the higher potential set, 0.61 V/0.50 V, gradually increased. This result is likely due to the increased concentration of Fc12-PF_6 in the lipid bilayer, dissolving from the aqueous channels. The peak potential attributed to the molecules incorporated into the lipid bilayer interface also shifted slightly from 0.61 V/0.50 V (1st cycle) to 0.63 V/0.48 V (200th cycle).

To remove the additional complications that this phenomenon adds to our analysis, in our subsequent experiments the amount of Fc12-PF_6 was lowered to 2% where the additional pair of lower-potential peaks at 0.42 V/0.31 V are absent (see **Figure 8b**).

The stability test of repeated redox cycling for 2%Fc12-PF_6 is shown in **Figure 8b**, only a single set of redox peaks was observed at 0.61 V/0.50 V, confirming that Fc12-PF_6 molecules diffused through the lipid/aqueous interface. Furthermore, the redox activity of the Fc12-PF_6 did not

degrade over continuous redox cycling. As displayed in **Figure 8b**, almost 90% of the anodic peak current was retained after 200th cycle.

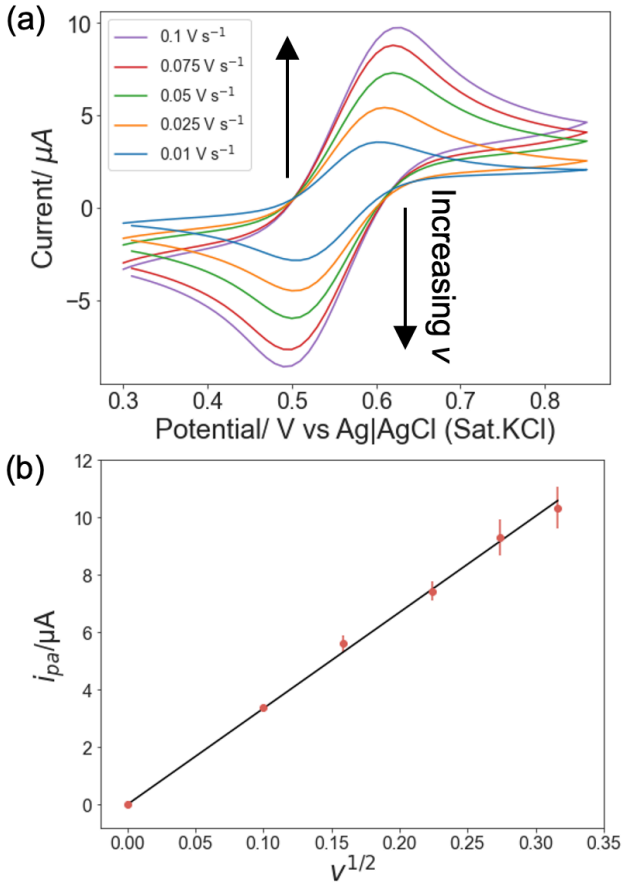

Figure 9. (a) Cyclic voltammograms of 2%Fc12-PF_6/MO modified electrode in H_2O PB recorded at five varying voltage scan rates: 0.1 V s^{-1}, 0.075 V s^{-1}, 0.05 V s^{-1}, 0.025 V s^{-1} and 0.01 V s^{-1}, and (b) Randle-Sevick plot: anodic peak currents (i_{pa}) vs square root of the scan rate ($v^{1/2}$), n=3

To measure the diffusion coefficient of Fc12-PF_6 within MO cubic phase, cyclic voltammograms with varying scan rates were recorded (see **Figure 9a**). The concentration of Fc12-PF_6 was estimated as per Kostela *et al* [61], in which the MO cubic phase was treated as a homogenous

medium. A 2% (w/w) weight of Fc12 was estimated to have a molar concentration of 10.9 mM over the total volume of the thin film. The geometric area of the electrode, 0.0314 cm^2, was considered as the active electrode surface area.

As shown in **Figure 9b**, the anodic peak current increases linearly with the square root of the scan rate, confirming that the mass transport of the Fc12-PF_6 is under diffusion control. [51] The diffusion coefficient of Fc12-PF_6 was calculated as $2.0 \pm 0.2 \times 10^{-8}$ cm^2 s^{-1}. These results align with the 0.2%Fc12-Br/MO.[21] The electrochemical activity of 0.2%Fc12-PF_6/MO resulted to be comparable to 0.2%Fc12-Br/MO (see SI Figure 3).

Fc12-PF_6/MO as a host medium to accommodate GOx for biosensing activities

The structure integrity of 2%Fc12-PF_6/MO and 2%Fc12-PF_6/MO/GOx lipid cubic phases in excess PB condition were examined using SAXS (see **Figure 10a**). All samples exhibited the characteristic patterns of a Pn3m cubic phase. First, the SAXS patterns between MO with and without the presence of 2%Fc12-PF_6 were compared. In the presence of Fc12-PF_6, the Bragg peaks of MO slightly shift towards high-q region by 0.03 Å. However, upon hosting GOx the shrinking effect caused by Fc12-PF_6 was less pronounced and the lattice dimension of 2%Fc12-PF_6/MO/GOx reverted to algin with that of MO.

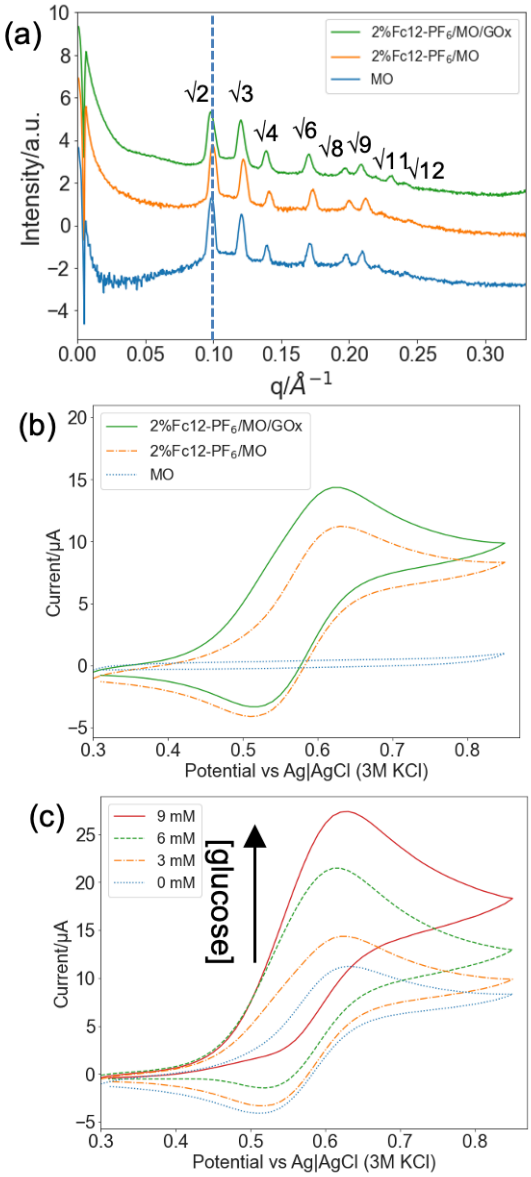

Figure 10. (a) SAXS patterns of MO, 2%Fc12-PF6/MO and 2%Fc12-PF6/MO in excess PB solution, the inserted dash line represents the √2 peak position of the MO SAXS pattern, (b) control tests: cyclic voltammograms recorded at 0.1 V s^{-1} for MO-, 2%Fc12-PF6/MO and 2%Fc12-PF6/MO modified disk electrodes soaked in 3 mM glucose PB solution, and (c) cyclic voltammograms of 2%Fc12-PF_6/MO/GOx modified disk electrode recorded at 0.1 V s^{-1} in PB solutions with varying glucose concentrations: 0 mM, 3 mM, 6 mM and 9 mM.

Figure 10b shows the CV tests in the presence of 3 mM glucose obtained with 2%Fc12-PF_6/MO/GOx, 2% Fc12-PF_6/MO and MO. As shown, both 2%Fc12-PF_6/MO and MO assay did not display any sign of electrocatalytic events, wherein the former adopts a classic reversible shape[53] with a set of redox peaks (i_{pa}/i_{pc}=1) and the latter does not have redox peaks at all. This result demonstrates that, contrary to 2%Fc12-PF_6/MO/GOx, both 2%Fc12-PF_6/MO and MO are inert to glucose oxidations. The anodic peak current ratio to cathodic peak current, i_{pa}/i_{pc}, observed with 2%Fc12-PF_6/MO/GOx was 1.4, which is intrinsically different from 2%Fc12-PF_6/MO. This could be due to the oxidized Fc12-PF_6 being taken up and reduced by GOx to trigger glucose oxidations, thus the flux of oxidized Fc12-PF_6 to interact with the electrode was decreased. Meanwhile the flux of reduced Fc12-PF_6 increased near the electrode and resulted in increased anodic currents. As shown in **Figure 10c**, the anodic current generated by 2%Fc12-PF_6/MO/GOx increased with the glucose concentration, which demonstrates the feasibility of applying 2%Fc12-PF_6/MO/GOx modified electrodes for glucose sensing.

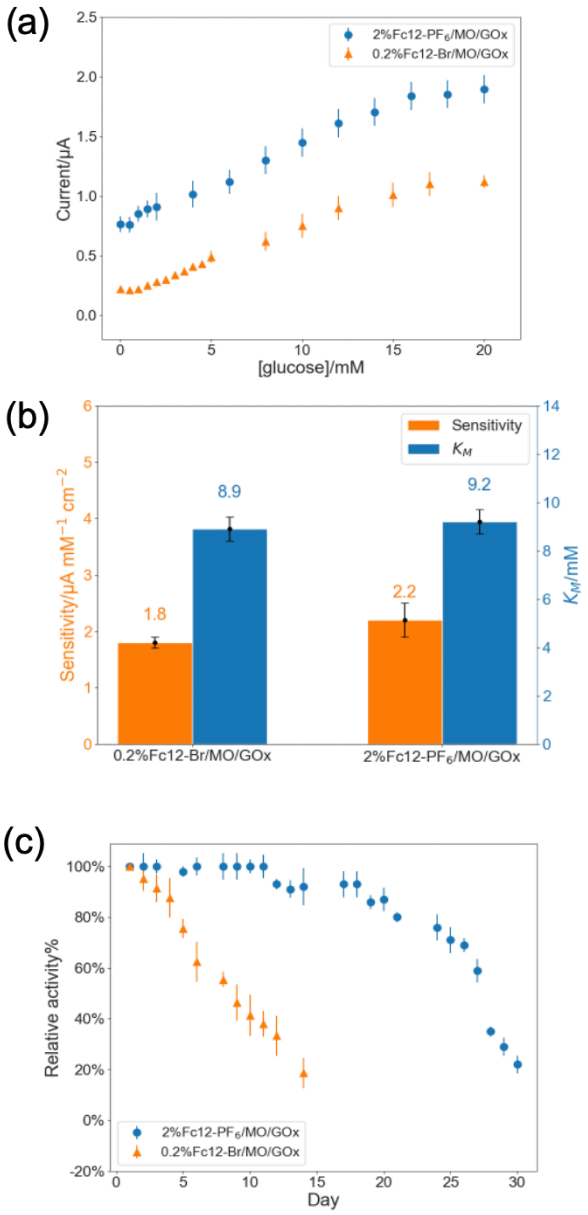

Figure 11. (a) Amperometric response of 2%Fc12-PF6/GOx/MO and 0.2%Fc12-Br/GOx/MO bioelectrodes in PB solutions (pH=7.0) with various glucose concentration, ranging from 0-20 mM, (b) comparisons of sensitivity and K_M between the Fc12-Br and the Fc12-PF_6 bioelectrodes, and (c) relative activity of Fc12-PF_6/MO/GOx and Fc12-Br/MO/GOx over 15 and 30 days respectively (n=3)

As shown in **Figure 11a**, a linear response to glucose was observed within the range 2-18 mM. The electrode sensitivity to glucose resulted to be 2.2 ± 0.5 μA mM^{-1} cm^{-2} and the Michaelis-Menten constant (K_M) was found to be 9.2 ± 0.2 mM.

To evaluate the performance of 2%Fc12-PF_6/MO/GOx, a comparison was made with the previously reported Fc12-Br bioelectrode system[21] (see **Figure 11b**). Surprisingly, despite the 2%Fc12-PF_6/MO/GOx system had employed higher %wt redox probe, both sensitivity and K_M did not display significant differences between the two types of the systems. The fact that these enzymatic kinetics results looked comparable suggests that the concentration of redox probe may not be the limiting factor affecting the magnitudes of the amperometric response. Instead, it is possible that the concentration of the enzyme entrapped within the medium plays a more crucial role.

The stability and relative activity of the Fc12-PF_6/MO/GOx bioelectrode were monitored over a period of 30 days, and the results are presented in **Figure 11c**. Notably, during the first 10 days of the measurement period, the relative activity remained close to 100%. In contrast, the earlier system Fc12-Br/MO/GOx lost 60 % of its activity by day 10.

Furthermore, even the MO entrapped GOx with no additional redox shuttle was previously reported to only maintain 100% activity for the first 5 days.[36] An explanation for this prolonged stability is the Hofmeister effect induced by $PF6^-$ within the water channel, which may lead to a reduction in the protein/aqueous interfacial tension, or a reduction in water channel size, either of which in turn could slower down the denaturing or unfolding process GOx. [62]

As shown in **Figure 11c**, after 10 days the relative activity of Fc12-PF_6/MO/GOx gradually decayed, reaching a reduction up to 80% after 20 days and up to 20% after 30 days of operation.

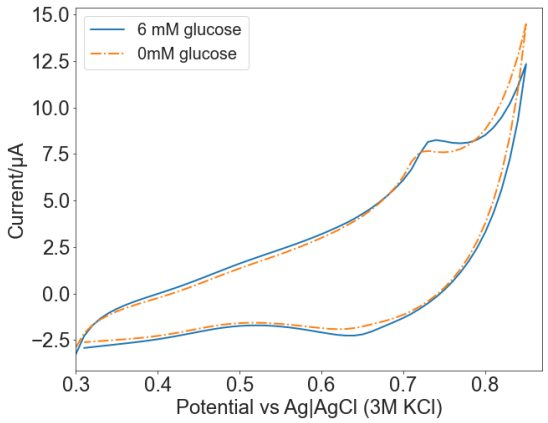

Figure 12. The cyclic voltammogram of Fc12-PF6/MO/GOx recorded at 0.1 V s^{-1} in the presence or absence of 6 mM glucose in PB solution (pH 7.0) after running relative activity for 30 days

To investigate whether GOx unfolding was the cause of the activity decay, a cyclic voltammogram was recorded on day 30 of the stability test. If the decrease in activity was solely due to GOx losing functionality, a reversible voltammogram (see **Figure 10b**) should still have been observed in the presence or absence of glucose. However, as seen in **Figure 12**, the appearance of the voltammogram changed after 30 days, with no reversible current peaks, and the oxidative potential shifted from 0.61 V to 0.72 V. CV scans at different scan rates (SI Figure 4) show that the magnitude of the anodic peak current has a linear dependence with the applied voltage scan rates, which suggests that the mass transport of Fc12-PF_6 is no longer under diffusional control.

The addition of 6 mM glucose to the electrolyte caused no changes to the CV curve. Thethe decreasing relative activity of the bioelectrode overtime could thus be attributed to both the diminishing diffusivity of the Fc12-PF_6 and the declining activity of the entrapped GOx.

CONCLUSION

Lyotropic lipid cubic phases formed by monoolein offer promise as host media for enzymes in biomedical device applications. LCPs deposition onto an electrode and its doping with an amphiphilic redox shuttle imparts electrochemical properties to the material. When a redox enzyme is entrapped within the lipid/redox shuttle structure, effective enzyme-based bioelectrodes are generated, for direct application onto transducer surfaces in novel biosensing applications. This protocol is efficient and cost-effective, simplifying electrode fabrication processes, and enabling the storage of bioelectrodes at room temperature.

The electrochemical reversibility of the inserted redox probe plays a crucial role in the stability of the system. Our study reveals that Fc12-Br/MO lost electrochemical reversibility over continuous redox cycles, which hinders its potential as a biosensing platform. Through, *in-situ* SANS experiments, we identified the localization of Fc12-Br molecules within the MO cubic phase during potential-hold and continuous electrochemical cycling. Although no leaching of Fc12-Br or localized phase transitions were observed, the Br^- counterions induced the formation of layer at the electrode surface that we propose is linked to the decay in electrochemical signals. Thus, counter ion metathesis was performed resulting in Fc12-PF_6.

The results shown that the MO cubic phase maintained structural integrity with the presence of Fc12-PF_6, and that electrochemical stability was improved. Moreover, this newly formed material was capable of hosting GOx for novel glucose sensing activities. When stored the Fc12-PF_6/MO/GOx at room in PB solutions temperature, it retained more than 80% relative activity over 20 days. This enhanced stability represents a significant improvement compared to the Fc12-Br

system and other nanomaterials[14], overcoming a major barrier to the more widespread adoption of these systems in biosensing applications.

ASSOCIATED CONTENT

Supporting Information.

Neutron beam SLD calculations for dynamically contrast matching; the *in-situ* SANS experimental set-up; pseudo reference electrode potential normalization; diffusivity study of Fc12-PF_6 within 0.2%Fc12-PF_6/MO; diffusivity study of Fc12-PF_6 within Fc12-PF_6/MO/GOx bioelectrode after 30 days.

AUTHOR INFORMATION

Corresponding Author

Adam M. Squires − *Department of Chemistry, University of Bath, Bath BA2 7AY, U.K.;*

orcid.org/0000- 0003-1396-467X*; Email:* **a.squires@bath.ac.uk**

Author Contributions

The manuscript was written through contributions of all authors.

ACKNOWLEDGMENT

We acknowledge beamtime allocation RB2220580 on ZOOM at ISIS Neutron and Muon Source, Didcot, U.K., DOI: 10.5286/ISIS.E. RB2220580-1.

ABBREVIATIONS

d-MO, deuterated monoolein; MO, monoolein; Fc12-Br, dodecyl(ferrocenylmethyl)-dimethylammonium bromide; Fc12-PF6, dodecyl(ferrocenylmethyl)dimethylammonium

hexafluorophosphate; PB, phosphate buffer; SANS, small angle neutron scattering; SAXS, small angle x-ray scattering; SLD, scattering length density;

REFERENCES

(1) Kim, J.; Campbell, A. S.; de Ávila, B. E.-F.; Wang, J. Wearable biosensors for healthcare monitoring. *Nat. Biotechnol.* **2019**, *37* (4), 389-406. DOI: 10.1038/s41587-019-0045-y.
(2) Gonzalez-Solino, C.; Bernalte, E.; Bayona Royo, C.; Bennett, R.; Leech, D.; Di Lorenzo, M. Self-Powered Detection of Glucose by Enzymatic Glucose/Oxygen Fuel Cells on Printed Circuit Boards. *ACS Appl. Mater. Interfaces* **2021**, *13* (23), 26704-26711. DOI: 10.1021/acsami.1c02747 From NLM.
(3) Kim, J.; Jeerapan, I.; Sempionatto, J. R.; Barfidokht, A.; Mishra, R. K.; Campbell, A. S.; Hubble, L. J.; Wang, J. Wearable bioelectronics: Enzyme-based body-worn electronic devices. *Acc. Chem. Res.* **2018**, *51* (11), 2820-2828.
(4) Ghaffari, R.; Choi, J.; Raj, M. S.; Chen, S.; Lee, S. P.; Reeder, J. T.; Aranyosi, A. J.; Leech, A.; Li, W.; Schon, S. Soft wearable systems for colorimetric and electrochemical analysis of biofluids. *Adv. Funct. Mater.* **2020**, *30* (37), 1907269.
(5) Bollella, P. Porous Gold: A New Frontier for Enzyme-Based Electrodes. *Nanomaterials (Basel)* **2020**, *10* (4). DOI: 10.3390/nano10040722 From NLM.
(6) Guisan, J. M.; López-Gallego, F.; Bolivar, J. M.; Rocha-Martín, J.; Fernandez-Lorente, G. The Science of Enzyme Immobilization. In *Immobilization of Enzymes and Cells: Methods and Protocols*, Guisan, J. M., Bolivar, J. M., López-Gallego, F., Rocha-Martín, J. Eds.; Springer US, 2020; pp 1-26.
(7) Zafar, H.; Channa, A.; Jeoti, V.; Stojanović, G. M. Comprehensive Review on Wearable Sweat-Glucose Sensors for Continuous Glucose Monitoring. *Sensors (Basel)* **2022**, *22* (2). DOI: 10.3390/s22020638 From NLM.
(8) Sehit, E.; Altintas, Z. Significance of nanomaterials in electrochemical glucose sensors: An updated review (2016-2020). *Biosens. Bioelectron.* **2020**, *159*, 112165. DOI: https://doi.org/10.1016/j.bios.2020.112165.
(9) Medina-Castillo, A. L.; Ruzic, L.; Nidetzky, B.; Bolivar, J. M. Hydrophilic Nonwoven Nanofiber Membranes as Nanostructured Supports for Enzyme Immobilization. *ACS Applied Polymer Materials* **2022**, *4* (8), 6054-6066. DOI: 10.1021/acsapm.2c00863.
(10) Aoki, K.; Saito, N. Biocompatibility and Carcinogenicity of Carbon Nanotubes as Biomaterials. *Nanomaterials* **2020**, *10* (2), 264.
(11) Zhu, S.; Luo, F.; Li, J.; Zhu, B.; Wang, G.-X. Biocompatibility assessment of single-walled carbon nanotubes using Saccharomyces cerevisiae as a model organism. *Journal of Nanobiotechnology* **2018**, *16* (1), 44. DOI: 10.1186/s12951-018-0370-1.
(12) Nezakati, T.; Seifalian, A.; Tan, A.; Seifalian, A. M. Conductive Polymers: Opportunities and Challenges in Biomedical Applications. *Chem. Rev.* **2018**, *118* (14), 6766-6843. DOI: 10.1021/acs.chemrev.6b00275.
(13) Setti, L.; Fraleoni-Morgera, A.; Ballarin, B.; Filippini, A.; Frascaro, D.; Piana, C. An amperometric glucose biosensor prototype fabricated by thermal inkjet printing. *Biosens. Bioelectron.* **2005**, *20* (10), 2019-2026. DOI: https://doi.org/10.1016/j.bios.2004.09.022.

(14) Li, G.; Wen, D. Sensing nanomaterials of wearable glucose sensors. *Chin. Chem. Lett.* **2021**, *32* (1), 221-228. DOI: https://doi.org/10.1016/j.cclet.2020.10.028.
(15) Cai, Y.; Tu, T.; Li, T.; Zhang, S.; Zhang, B.; Fang, L.; Ye, X.; Liang, B. Research on direct electron transfer of native glucose oxidase at PEDOT:PSS hydrogels modified electrode. *J. Electroanal. Chem.* **2022**, *922*, 116738. DOI: https://doi.org/10.1016/j.jelechem.2022.116738.
(16) Wilson, G. S. Native glucose oxidase does not undergo direct electron transfer. *Biosens. Bioelectron.* **2016**, *82*, vii-viii. DOI: https://doi.org/10.1016/j.bios.2016.04.083.
(17) Zhao, Y.; Liu, B.; Pan, L.; Yu, G. 3D nanostructured conductive polymer hydrogels for high-performance electrochemical devices. *Energy & Environmental Science* **2013**, *6* (10), 2856-2870, 10.1039/C3EE40997J. DOI: 10.1039/C3EE40997J.
(18) Zahed, M. A.; Barman, S. C.; Das, P. S.; Sharifuzzaman, M.; Yoon, H. S.; Yoon, S. H.; Park, J. Y. Highly flexible and conductive poly (3, 4-ethylene dioxythiophene)-poly (styrene sulfonate) anchored 3-dimensional porous graphene network-based electrochemical biosensor for glucose and pH detection in human perspiration. *Biosens. Bioelectron.* **2020**, *160*, 112220. DOI: https://doi.org/10.1016/j.bios.2020.112220.
(19) Qiu, H.; Caffrey, M. The phase diagram of the monoolein/water system: metastability and equilibrium aspects. *Biomaterials* **2000**, *21* (3), 223-234. DOI: https://doi.org/10.1016/S0142-9612(99)00126-X.
(20) Briggs, J.; Caffrey, M. The temperature-composition phase diagram and mesophase structure characterization of monopentadecenoin in water. *Biophys. J.* **1994**, *67* (4), 1594-1602. DOI: https://doi.org/10.1016/S0006-3495(94)80632-0.
(21) Liu, W.; Lewis, S. E.; di Lorenzo, M.; Squires, A. M. Development of Redox-Active Lyotropic Lipid Cubic Phases for Biosensing Platforms. *Langmuir* **2023**. DOI: 10.1021/acs.langmuir.3c02307.
(22) Kulkarni, C. V.; Wachter, W.; Iglesias-Salto, G.; Engelskirchen, S.; Ahualli, S. Monoolein: a magic lipid? *Phys. Chem. Chem. Phys.* **2011**, *13* (8), 3004-3021, 10.1039/C0CP01539C. DOI: 10.1039/C0CP01539C.
(23) Han, L.; Che, S. An Overview of Materials with Triply Periodic Minimal Surfaces and Related Geometry: From Biological Structures to Self-Assembled Systems. *Adv. Mater.* **2018**, *30* (17), 1705708. DOI: https://doi.org/10.1002/adma.201705708.
(24) Hyde, S.; Ninham, B. W.; Andersson, S.; Larsson, K.; Landh, T.; Blum, Z.; Lidin, S. Chapter 1 - The Mathematics of Curvature. In *The Language of Shape*, Hyde, S., Ninham, B. W., Andersson, S., Larsson, K., Landh, T., Blum, Z., Lidin, S. Eds.; Elsevier Science B.V., 1997; pp 1-42.
(25) Tenchov, B. G.; MacDonald, R. C.; Lentz, B. R. Fusion peptides promote formation of bilayer cubic phases in lipid dispersions. An x-ray diffraction study. *Biophys. J.* **2013**, *104* (5), 1029-1037. DOI: 10.1016/j.bpj.2012.12.034 From NLM.
(26) Michielsen, K.; Stavenga, D. G. Gyroid cuticular structures in butterfly wing scales: biological photonic crystals. *Journal of The Royal Society Interface* **2008**, *5* (18), 85-94. DOI: doi:10.1098/rsif.2007.1065.
(27) Mezzenga, R.; Seddon, J. M.; Drummond, C. J.; Boyd, B. J.; Schröder-Turk, G. E.; Sagalowicz, L. Nature-Inspired Design and Application of Lipidic Lyotropic Liquid Crystals. *Adv. Mater.* **2019**, *31* (35), 1900818. DOI: https://doi.org/10.1002/adma.201900818.
(28) Conn, C. E.; Drummond, C. J. Nanostructured bicontinuous cubic lipid self-assembly materials as matrices for protein encapsulation. *Soft Matter* **2013**, *9* (13), 3449-3464, 10.1039/C3SM27743G. DOI: 10.1039/C3SM27743G.

(29) Zabara, A.; Chong, J. T. Y.; Martiel, I.; Stark, L.; Cromer, B. A.; Speziale, C.; Drummond, C. J.; Mezzenga, R. Design of ultra-swollen lipidic mesophases for the crystallization of membrane proteins with large extracellular domains. *Nat. Commun.* **2018**, *9* (1), 544. DOI: 10.1038/s41467-018-02996-5.
(30) Esposito, E.; Carducci, F.; Mariani, P.; Huang, N.; Simeliere, F.; Cortesi, R.; Romeo, G.; Puglia, C. Monoolein liquid crystalline phases for topical delivery of crocetin. *Colloids and Surfaces B-Biointerfaces* **2018**, *171*, 67-74. DOI: 10.1016/j.colsurfb.2018.07.011.
(31) Kulkarni, C. V.; Vishwapathi, V. K.; Quarshie, A.; Moinuddin, Z.; Page, J.; Kendrekar, P.; Mashele, S. S. Self-Assembled Lipid Cubic Phase and Cubosomes for the Delivery of Aspirin as a Model Drug. *Langmuir* **2017**, *33* (38), 9907-9915. DOI: 10.1021/acs.langmuir.7b02486.
(32) Chountoulesi, M.; Pippa, N.; Pispas, S.; Chrysina, E. D.; Forys, A.; Trzebicka, B.; Demetzos, C. Cubic lyotropic liquid crystals as drug delivery carriers: Physicochemical and morphological studies. *Int. J. Pharm.* **2018**, *550* (1-2), 57-70. DOI: 10.1016/j.ijpharm.2018.08.003.
(33) Nazaruk, E.; Sadowska, K.; Madrak, K.; Biernat, J. F.; Rogalski, J.; Bilewicz, R. Composite Bioelectrodes Based on Lipidic Cubic Phase with Carbon Nanotube Network. *Electroanalysis* **2009**, *21* (3-5), 507-511, Article; Proceedings Paper. DOI: 10.1002/elan.200804435.
(34) Zatloukalova, M.; Nazaruk, E.; Novak, D.; Vacek, J.; Bilewicz, R. Lipidic liquid crystalline cubic phases for preparation of ATP-hydrolysing enzyme electrodes. *Biosens. Bioelectron.* **2018**, *100*, 437-444, Article. DOI: 10.1016/j.bios.2017.09.036.
(35) Vallooran, J. J.; Handschin, S.; Pillai, S. M.; Vetter, B. N.; Rusch, S.; Beck, H.-P.; Mezzenga, R. Lipidic Cubic Phases as a Versatile Platform for the Rapid Detection of Biomarkers, Viruses, Bacteria, and Parasites. *Adv. Funct. Mater.* **2016**, *26* (2), 181-190. DOI: https://doi.org/10.1002/adfm.201503428.
(36) Nylander, T.; Mattisson, C.; Razumas, V.; Miezis, Y.; Håkansson, B. A study of entrapped enzyme stability and substrate diffusion in a monoglyceride-based cubic liquid crystalline phase. *Colloids and Surfaces A: Physicochemical and Engineering Aspects* **1996**, *114*, 311-320. DOI: https://doi.org/10.1016/0927-7757(96)03563-7.
(37) ENGSTRÖM, S.; HÅKANSON, H.; MANDENIUS, C. F. Enzyme Stabilization in Composite Cubic Phases. *Ann. N.Y. Acad. Sci.* **1990**, *613* (1), 429-430. DOI: https://doi.org/10.1111/j.1749-6632.1990.tb18193.x.
(38) Saji, T.; Hoshino, K.; Aoyagui, S. Reversible formation and disruption of micelles by control of the redox state of the head group. *J. Am. Chem. Soc.* **1985**, *107* (24), 6865-6868.
(39) Kostela, J.; Elmgren, M.; Almgren, M. Electrochemical properties and diffusion of a redox active surfactant incorporated in bicontinuous cubic and lamellar phase. *Electrochim. Acta* **2005**, *50* (16), 3333-3340. DOI: https://doi.org/10.1016/j.electacta.2004.12.006.
(40) Donohue, J. J.; Buttry, D. A. Adsorption and micellization influence the electrochemistry of redox surfactants derived from ferrocene. *Langmuir* **1989**, *5* (3), 671-678.
(41) Randle, R. I.; Fuentes-Caparrós, A. M.; Cavalcanti, L. P.; Schweins, R.; Adams, D. J.; Draper, E. R. Investigating Aggregation Using In Situ Electrochemistry and Small-Angle Neutron Scattering. *The Journal of Physical Chemistry C* **2022**, *126* (31), 13427-13432. DOI: 10.1021/acs.jpcc.2c03210.
(42) Draper, E. R. Electrochemical cell for neutron scattering. *Nature Reviews Chemistry* **2023**, *7* (10), 667-667. DOI: 10.1038/s41570-023-00544-4.

(43) Yu, X.; Cheng, Y.; Li, Y.; Polo-Garzon, F.; Liu, J.; Mamontov, E.; Li, M.; Lennon, D.; Parker, S. F.; Ramirez-Cuesta, A. J.; et al. Neutron Scattering Studies of Heterogeneous Catalysis. *Chem. Rev.* **2023**. DOI: 10.1021/acs.chemrev.3c00101.
(44) Jeffries, C. M.; Ilavsky, J.; Martel, A.; Hinrichs, S.; Meyer, A.; Pedersen, J. S.; Sokolova, A. V.; Svergun, D. I. Small-angle X-ray and neutron scattering. *Nature Reviews Methods Primers* **2021**, *1* (1), 70. DOI: 10.1038/s43586-021-00064-9.
(45) van 't Hag, L.; de Campo, L.; Garvey, C. J.; Feast, G. C.; Leung, A. E.; Yepuri, N. R.; Knott, R.; Greaves, T. L.; Tran, N.; Gras, S. L.; et al. Using SANS with Contrast-Matched Lipid Bicontinuous Cubic Phases To Determine the Location of Encapsulated Peptides, Proteins, and Other Biomolecules. *The Journal of Physical Chemistry Letters* **2016**, *7* (14), 2862-2866. DOI: 10.1021/acs.jpclett.6b01173.
(46) Angelov, B.; Angelova, A.; Garamus, V. M.; Lebas, G.; Lesieur, S.; Ollivon, M.; Funari, S. S.; Willumeit, R.; Couvreur, P. Small-Angle Neutron and X-ray Scattering from Amphiphilic Stimuli-Responsive Diamond-Type Bicontinuous Cubic Phase. *J. Am. Chem. Soc.* **2007**, *129* (44), 13474-13479. DOI: 10.1021/ja072725+.
(47) Hwang, D.-W.; Lee, S.; Seo, M.; Chung, T. D. Recent advances in electrochemical non-enzymatic glucose sensors – A review. *Anal. Chim. Acta* **2018**, *1033*, 1-34. DOI: https://doi.org/10.1016/j.aca.2018.05.051.
(48) Facci, J. S.; Falcigno, P. A.; Gold, J. M. Characterization of electroactive Langmuir-Blodgett monolayers of (ferrocenylmethyl) dimethyloctadecylammonium sulfate at gold and air/water interfaces. *Langmuir* **1986**, *2* (6), 732-738.
(49) Tyler, A. I. I.; Barriga, H. M. G.; Parsons, E. S.; McCarthy, N. L. C.; Ces, O.; Law, R. V.; Seddon, J. M.; Brooks, N. J. Electrostatic swelling of bicontinuous cubic lipid phases. *Soft Matter* **2015**, *11* (16), 3279-3286, 10.1039/C5SM00311C. DOI: 10.1039/C5SM00311C.
(50) Nazaruk, E.; Smolinski, S.; Swatko-Ossor, M.; Ginalska, G.; Fiedurek, J.; Rogalski, J.; Bilewicz, R. Enzymatic biofuel cell based on electrodes modified with lipid liquid-crystalline cubic phases. *J. Power Sources* **2008**, *183* (2), 533-538, Article. DOI: 10.1016/j.jpowsour.2008.05.061.
(51) Bard, A. J. *Electrochemical methods : fundamentals and applications*; New York

Chichester : John Wiley, 2001.
(52) Arnold, O.; Bilheux, J. C.; Borreguero, J. M.; Buts, A.; Campbell, S. I.; Chapon, L.; Doucet, M.; Draper, N.; Ferraz Leal, R.; Gigg, M. A.; et al. Mantid—Data analysis and visualization package for neutron scattering and μ SR experiments. *Nuclear Instruments and Methods in Physics Research Section A: Accelerators, Spectrometers, Detectors and Associated Equipment* **2014**, *764*, 156-166. DOI: https://doi.org/10.1016/j.nima.2014.07.029.
(53) Fisher, A. C. *Electrode dynamics*; Oxford : Oxford University Press, 1996.
(54) Shearman, G. C.; Ces, O.; Templer, R. H.; Seddon, J. M. Inverse lyotropic phases of lipids and membrane curvature. *J. Phys.: Condens. Matter* **2006**, *18* (28), S1105. DOI: 10.1088/0953-8984/18/28/S01.
(55) van 't Hag, L.; Gras, S. L.; Conn, C. E.; Drummond, C. J. Lyotropic liquid crystal engineering moving beyond binary compositional space – ordered nanostructured amphiphile self-assembly materials by design. *Chem. Soc. Rev.* **2017**, *46* (10), 2705-2731, 10.1039/C6CS00663A. DOI: 10.1039/C6CS00663A.
(56) Deakin, M. R.; Li, T. T.; Melroy, O. R. A study of the electrosorption of bromide and iodide ions on gold using the quartz crystal microbalance. *Journal of Electroanalytical Chemistry and*

Interfacial Electrochemistry **1988**, *243* (2), 343-351. DOI: https://doi.org/10.1016/0022-0728(88)80039-1.
(57) Király, Z.; Findenegg, G. H.; Mastalir, Á. Adsorption of Dodecyltrimethylammonium Bromide and Sodium Bromide on Gold Studied by Liquid Chromatography and Flow Adsorption Microcalorimetry. *Langmuir* **2006**, *22* (7), 3207-3213. DOI: 10.1021/la053184+.
(58) Gregory, K. P.; Elliott, G. R.; Robertson, H.; Kumar, A.; Wanless, E. J.; Webber, G. B.; Craig, V. S. J.; Andersson, G. G.; Page, A. J. Understanding specific ion effects and the Hofmeister series. *Phys. Chem. Chem. Phys.* **2022**, *24* (21), 12682-12718, 10.1039/D2CP00847E. DOI: 10.1039/D2CP00847E.
(59) Brasnett, C.; Longstaff, G.; Compton, L.; Seddon, A. Effects of Cations on the Behaviour of Lipid Cubic Phases. *Sci. Rep.* **2017**, *7* (1), 8229. DOI: 10.1038/s41598-017-08438-4.
(60) Mazzini, V.; Craig, V. S. J. What is the fundamental ion-specific series for anions and cations? Ion specificity in standard partial molar volumes of electrolytes and electrostriction in water and non-aqueous solvents. *Chem. Sci.* **2017**, *8* (10), 7052-7065, 10.1039/C7SC02691A. DOI: 10.1039/C7SC02691A.
(61) Kostela, J.; Elmgren, M.; Kadi, M.; Almgren, M. Redox activity and diffusion of hydrophilic, hydrophobic, and amphiphilic redox active molecules in a bicontinuous cubic phase. *J. Phys. Chem. B* **2005**, *109* (11), 5073-5078. DOI: 10.1021/jp048088g From NLM.
(62) Sedlák, E.; Sedláková, D.; Marek, J.; Hančár, J.; Garajová, K.; Žoldák, G. Ion-Specific Protein/Water Interface Determines the Hofmeister Effect on the Kinetic Stability of Glucose Oxidase. *The Journal of Physical Chemistry B* **2019**, *123* (38), 7965-7973. DOI: 10.1021/acs.jpcb.9b05195.